Low Frequency Current Ripple Mitigation of Two Stage Three-Phase PEMFC Generation Systems

Huiwen Deng[*], Qi Li[†], Zhixiang Liu[*], Lun Li[*], and Weirong Chen[*]

[*,†]School of Electrical Engineering, Southwest Jiaotong University, Chengdu, China

Abstract

This paper presents a two stage three-phase proton exchange membrane fuel cell (PEMFC) generation system. When the system is connected to a three-phase load, it is very sensitive to the characteristics and type of the load. Especially unbalanced three-phase loads, which result in a pulsating power that is twice the output frequency at the inverter output, and cause the dc-link to generate low frequency ripples. This penetrates to the fuel cell side through the front-end dc-dc converter, which makes the fuel cell work in an unsafe condition and degrades its lifespan. In this paper, the generation and propagation mechanism of low frequency ripple is analyzed and its impact on fuel cells is presented based on the PEMFC output characteristics model. Then a novel method to evaluate low frequency current ripple control capability is investigated. Moreover, a control scheme with bandpass filter inserted into the current feed-forward path, and ripple duty ratio compensation based on current mode control with notch filter is also proposed to achieve low frequency ripple suppression and dynamic characteristics improvement during load transients. Finally, different control methods are verified and compared by simulation and experimental results.

Key words: Duty ratio compensation, Low frequency ripple suppression, PEMFC generation system, Unbalanced three-phase load

I. Introduction

The fuel cell is referred to as one of the most important generation systems of the 21st century in many existing generation technologies after fossil power, hydro power and nuclear power generations, which can convert chemical energy into electrical and thermal energy without harmful gas emissions. With the advantages of a high energy conversion ratio (about 40%~60%), large current density, high specific power, and long cycle life, the PEMFC has been widely used in many areas [1]. Since the PEMFC has relatively soft output voltage characteristics, a power electronic circuit must be adopted to meet the needs of practical applications. There are many kinds of topologies for PEMFC generation systems. However, the choice of topology is not the point of this paper. This paper investigates a two stage generation system which is quite suitable for fuel cell applications [2], [3]. As shown in Fig. 1, the front-end dc-dc converter converts input voltage into a desired dc-link voltage for the downstream three-phase dc-ac inverter, the three-phase inverter converts the dc-link voltage into an appropriate ac voltage, and the LC filter achieves sine wave of the output voltage waveforms. The dc-ac inverter can be connected to a three-phase load (stand-alone mode) or power grid with ac connectors (grid-connected mode). When the PEMFC generation system operates in stand-alone mode, the unbalanced three-phase load will produce pulsating power that is double the output frequency at the inverter output, causing the dc-link to generate low frequency ripple [4]. This inversely penetrates to the fuel cell through the front-end dc-dc converter. Thus, the fuel cell output voltage changes with the pulsating output current, which significantly affects the hydrogen utilization, durability and lifetime of the fuel cell stack. In addition, the pulsating current can also lead to conduction losses of the system, which increases the current stress on the power switches [5]-[9]. With the fuel cell mathematic model, the low frequency current ripple is concluded to be more serious than the low frequency voltage ripple. Therefore, the low frequency current ripple should be suppressed.

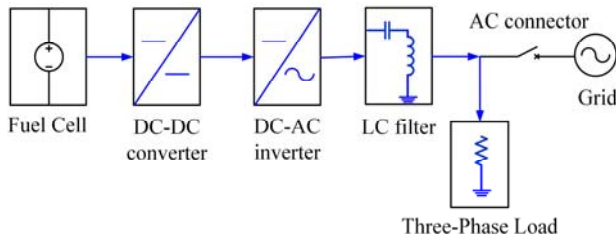Recently, various kinds of methods to suppress low

Fig. 1. Block diagram of PEMFC generation system.

frequency current ripple have been presented in [10]-[21], which can be divided into two categories, namely passive and active suppression methods. In the passive methods, extra large-scale dc-link electrolytic capacitor or energy storage devices are needed. Using these methods makes increasing the dc-link capacitance to reduce the current ripple simple and convenient [13]. However, an electrolytic capacitor dramatically increases the volume of the dc-dc converter, and without proper control the current ripple may still be high even though the capacitance is large enough. In [11]-[16], a bi-directional dc-dc converter in parallel with the dc-link is proposed. This converter is controlled to supply pulsating power by a supercapacitor or battery, while the fuel cell can provide steady output power. These methods are effective but an extra converter results in higher cost, higher power loss and lower efficiency. Active methods have also been presented in the literature. In [10] the current mode control was first proposed. With the regulation of the voltage loop crossover frequency, suppression of the low frequency current ripple can be achieved. Unfortunately, the dynamic performance during load transients is not satisfactory. A novel waveform control (WCF) technique based on a differential inverter is studied in [19]-[21]. By controlling the waveforms of the capacitors, the low frequency current ripple can be reduced and good dynamic performance can be achieved. However, this method is only suitable for a specific topology, and a fourth-order current ripple arises at the input side. The authors of [17] and [18] show that from the point of view of the virtual impedance, by adding a virtual impedance to the front-end dc-dc converter to increase the equivalent impedance, the low frequency current ripple can be reduced. However, the dynamic performance and current ripple suppression are in conflict. Therefore, a tradeoff between the current ripple and the dynamic performance must be considered. Based on the above analysis, a novel method with bandpass filter inserted into the current feed-forward path and ripple duty ratio compensation based on current mode control with a notch filter (CMC+VLN+CFBRC) has been proposed in this paper. It can realize current ripple suppression and dynamic performance improvement. In addition, the comprehensive performance is optimal.

This paper is organized as follows. The generation and propagation mechanism of the low frequency current ripple is analyzed in Section II. In Section III, the impact of current ripple on fuel cells is presented based on PEMFC output characteristics model. In Section IV, ripple suppression gain is proposed to evaluate the low frequency current ripple control capability. Then, a current mode control (CMC) method and current mode control with notch filter in the voltage loop (CMC+VLN) method are investigated. In Section V, the proposed CMC+VLN+CFBRC method is compared with the CMC+VLN and a method based on CMC+VLN is presented by adding a current feed-forward with notch filter in the branch (CMC+VLN+CFN). It is shown in an analysis that the CMC+VLN can realize good current ripple suppression but poor dynamic performance. It is also shown that the CMC+VLN+CFN has better dynamic performance, but worse current ripple suppression compared with the CMC+VLN. Meanwhile, the CMC+VLN+CFBRC achieves both current ripple suppression and dynamic performance improvement. In Section VI, experimental results verify the analyses presented in Section IV and V. Finally some conclusions are given in Section VII.

II. GENERATION AND PROPAGATION MECHANISM OF LOW FREQUENCY CURRENT RIPPLE

Fuel cell generation systems usually operate in the stand-alone mode or the grid-connected mode [4]. Fig.2 shows the schematic of a two stage three-phase fuel cell power conditioning system (FC-PCS). When the ac connecter S is off, the FC-PCS is disconnected from the grid in the stand-alone mode with a three-phase load. The relationship between the ac side and the dc-link side is firstly derived.

Let v_{dc} denotes the dc-link voltage that contains ripple. The dc-link capacitor C_{dc} is equivalent to two series-connected capacitors for the sake of convenience. The three-phase inverter input current is defined as i_{dc}, the output ac voltages and currents are defined as u_a, u_b, u_c and i_a, i_b, i_c, respectively. Supposing that the output waveforms are ideal sinusoidal waves, and neglecting the high switching frequency ripple, the output voltages of the inverter can be expressed as:

$$\begin{cases} u_a = U\sin(\omega t) \\ u_b = U\sin(\omega t - 2\pi/3) \\ u_c = U\sin(\omega t + 2\pi/3) \end{cases} \tag{1}$$

Where U is the amplitude of the output voltage, $\omega = 2\pi f$ is the angular frequency, f is the output frequency, and Z_a, Z_b, Z_c are the three-phase load impedances. The output currents of the inverter can be expressed by the following equations:
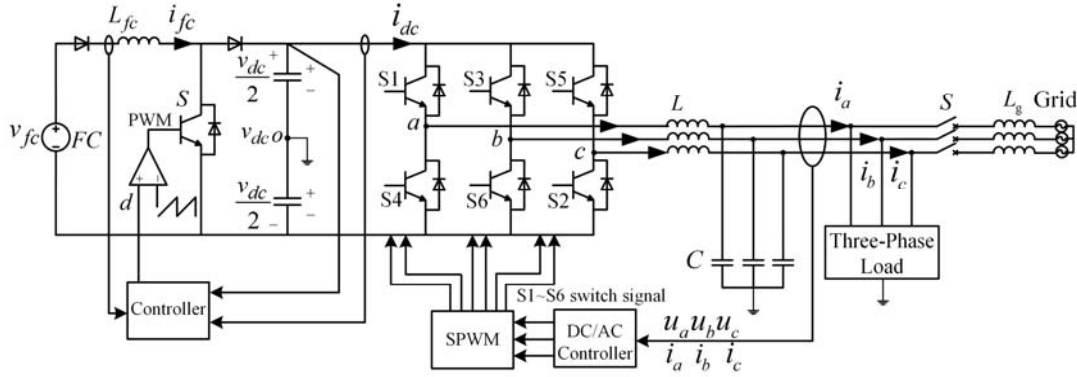
Fig. 2. PCS for fuel cell generation system.

$$\begin{cases} i_a = I_a \sin(\omega t + \varphi_a) \\ i_b = I_b \sin(\omega t - 2\pi/3 + \varphi_b) \\ i_c = I_c \sin(\omega t + 2\pi/3 + \varphi_c) \end{cases} \quad (2)$$

Where I_a, I_b, I_c are the three-phase output current amplitudes, and φ_a, φ_b, φ_c are the three-phase load impedance angles. According to (1) and (2), the three-phase instantaneous output power of the inverter can be given by:

$$\begin{cases} P_a = u_a i_a = U\sin(\omega t) \times I_a \sin(\omega t + \varphi_a) \\ P_b = u_b i_b = U\sin(\omega t - 2\pi/3) \times I_b \sin(\omega t - 2\pi/3 + \varphi_b) \\ P_c = u_c i_c = U\sin(\omega t + 2\pi/3) \times I_c \sin(\omega t + 2\pi/3 + \varphi_c) \end{cases} \quad (3)$$

The total output instantaneous power is shown as:

$$P = P_a + P_b + P_c \quad (4)$$

Substituting (3) into (4) yields:

$$\begin{aligned} P = &1/2U(I_a \cos\varphi_a + I_b \cos\varphi_b + I_c \cos\varphi_c) \\ &+ U(-1/2 I_a \cos\varphi_a + \sqrt{3}/4 I_b \sin\varphi_b + 1/4 I_b \cos\varphi_b \\ &+ 1/4 I_c \cos\varphi_c - \sqrt{3}/4 I_c \sin\varphi_c)\cos 2\omega t \\ &+ U(1/2 I_a \sin\varphi_a + \sqrt{3}/4 I_b \cos\varphi_b - 1/4 I_b \sin\varphi_b \\ &- 1/4 I_c \sin\varphi_c - \sqrt{3}/4 I_c \cos\varphi_c)\sin 2\omega t \end{aligned} \quad (5)$$

From (5), the three-phase load is balanced, that is $Z_a = Z_b = Z_c = Z$, $\varphi_a = \varphi_b = \varphi_c = \varphi$, and $I_a = I_b = I_c = I$. Equation (5) can be rewritten as:

$$P = \frac{3}{2}UI\cos\varphi \quad (6)$$

As can be seen from (6), in the balanced situation, the output instantaneous power is constant without pulsating. Therefore, there is no low frequency ripple. However, when the three-phase load is unbalanced, equation (5) can be expressed as:

$$P = P_d + P_{2nd}\cos(2\omega t - \varphi_{2nd}) \quad (7)$$

Where P_d is the dc component, P_{2nd} is the second-order pulsating component, and φ_{2nd} is the impedance angle. From (7) it can be concluded that in the unbalanced situation there exists second-order pulsating power in the output power. When the unbalance is more serious, the content of the low frequency ripple in P_{2nd} is higher. P_d, P_{2nd} and φ_{2nd} are shown as follows:

$$P_d = \frac{1}{2}U(I_a \cos\varphi_a + I_b \cos\varphi_b + I_c \cos\varphi_c) \quad (8)$$

$$\begin{aligned} P_{2nd} = U\big[&(-1/2 I_a \cos\varphi_a + \sqrt{3}/4 I_b \sin\varphi_b \\ &+ 1/4 I_b \cos\varphi_b + 1/4 I_c \cos\varphi_c - \sqrt{3}/4 I_c \sin\varphi_c)^2 \\ &+ (1/2 I_a \sin\varphi_a + \sqrt{3}/4 I_b \cos\varphi_b - 1/4 I_b \sin\varphi_b \\ &- 1/4 I_c \sin\varphi_c - \sqrt{3}/4 I_c \cos\varphi_c)^2\big] \end{aligned} \quad (9)$$

$$\begin{aligned} \varphi_{2nd} = \arctan\big(&(1/2 I_a \sin\varphi_a + \sqrt{3}/4 I_b \cos\varphi_b - 1/4 I_b \sin\varphi_b \\ &- 1/4 I_c \sin\varphi_c - \sqrt{3}/4 I_c \cos\varphi_c)/(-1/2 I_a \cos\varphi_a \\ &+ \sqrt{3}/4 I_b \sin\varphi_b + 1/4 I_b \cos\varphi_b + 1/4 I_c \cos\varphi_c \\ &- \sqrt{3}/4 I_c \sin\varphi_c)\big) \end{aligned} \quad (10)$$

Supposing the efficiency of the three-phase inverter is 100%, and neglecting the loss and reactive power, the following can be obtained:

$$P_{dc} = P \quad (11)$$

P_{dc} is the power that flows into the three-phase inverter. Supposing the voltage v_{dc} pulsates in a small range, it can be considered as constant V_{dc}, which will be discussed later. Therefore, the input current of the three-phase inverter is derived as:

$$i_{dc} = \frac{P_d}{V_{dc}} + \frac{P_{2nd}}{V_{dc}}\cos(2\omega t - \varphi_{2nd}) \quad (12)$$

i_{dc} contains two parts, $I_{dc} = P_d/V_{dc}$ is the dc component and $i_{2nd} = P_{2nd}/V_{dc}\cos(2\omega t - \varphi_{2nd})$ is the second-order ripple component. The front-end dc-dc converter of the FC-PCS is shown in Fig.3.

In Fig. 3, i_f is the output current of the front-end dc-dc converter, i_C is the dc-link capacitor branch current, C_{dc} is designed to filter switching frequency ripple, i_{fc} and v_{fc} are fuel cell output current and voltage. The second-order current ripple in i_{dc} flows through the two branches, i_f
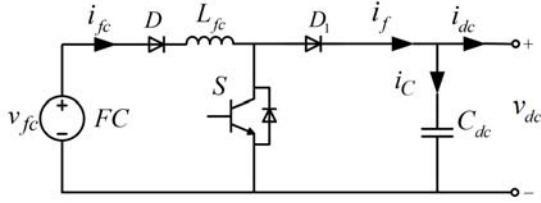
Fig. 3. Configuration of front-end dc-dc converter.

and i_C can be derived as:

$$\begin{cases} i_f = I_{dc} + \delta i_{2nd} \\ i_C = \beta i_{2nd} \end{cases} \quad (13)$$

Where δ, β are i_{2nd} the distribution coefficients of the two branches, and $\delta + \beta = 1$. When i_C flows through the capacitor branch, the pulsating voltage v_{2nd} is generated.

$$v_{dc} = V_{dc} + v_{2nd} \quad (14)$$

$$v_{2nd} = \frac{\beta P_{2nd}}{2\omega C_{dc} V_{dc}} \sin(2\omega t - \varphi_{2nd}) \quad (15)$$

From (15) it can be conclude that v_{2nd} is produced by i_{2nd}, and C_{dc} has a tremendous impact on the dc-link voltage. The bigger the capacitance of C_{dc} is, the smaller v_{2nd} becomes. Thus, the maximum value of v_{2nd} can be expressed as:

$$\Delta v_{2nd\_m} = \frac{\beta P_{2nd}}{\omega C_{dc} V_{dc}} \quad (16)$$

According to the authors of [22] and [23], if v_{2nd} is less than 4% of V_{dc}, the performance of the inverter is not significantly affected, and the THD of ac output voltage can be restrained in a small range regardless of the loads. Therefore, the capacitor should be chosen according to (17)

$$C_{dc} \geq \frac{\beta P_{2nd}}{\omega \Delta v_{2nd\_m} V_{dc}} \quad (17)$$

Assuming the fuel cell output voltage is constant, the duty ratio can be obtained by:

$$d = \frac{V_{dc} + v_{2nd}}{V_{fc}} = \alpha + \alpha_{2nd} \quad (18)$$

Where $\alpha = 1/(1-D)$, α_{2nd} is caused by second-order pulsation, and the fuel cell output current can be derived as:
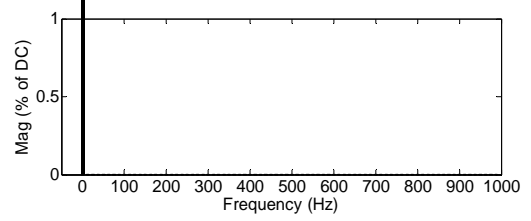
$$i_{fc} = i_f(\alpha + \alpha_{2nd}) \quad (19)$$

Substituting (13) into (19), i_{fc} can be rewritten as:

$$i_{fc} = I_{dc}\alpha + I_{dc}\alpha_{2nd} + \alpha\delta i_{2nd} + \delta i_{2nd}\alpha_{2nd} \quad (20)$$
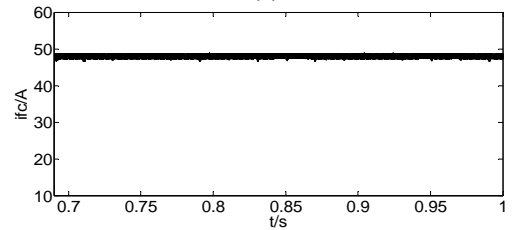
As can be seen from (20), i_{fc} contains the first dc component and three ac parts [18]. From (17) and (18), an appropriate dc-link capacitance can realize low voltage ripple. In this paper, the minimal capacitance is 729 μF. Therefore, 900 μF is chosen as the dc-link capacitance. The forth part
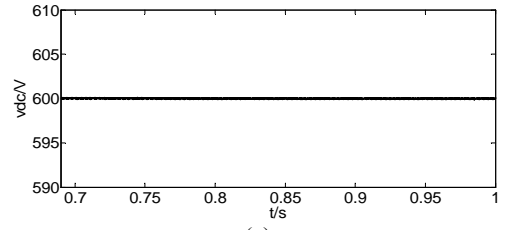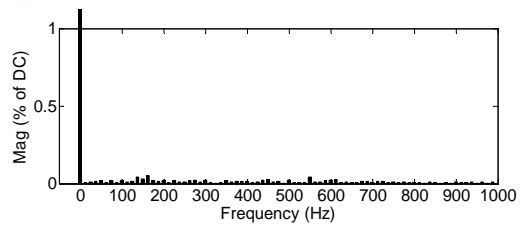

Fig.4. Key waveforms and FFT analysis in balanced situation. (a) DC-link voltage v_{dc}. (b) v_{dc} FFT analysis. (c) Fuel cell output current i_{fc}. (d) i_{fc} FFT analysis.

leading to the forth-order harmonic current caused by second-order pulsation can be neglected. Therefore, the following is obtained:

$$i_{fc} = I_{dc}\alpha + I_{dc}\alpha_{2nd} + \alpha\delta i_{2nd} \quad (21)$$

Fig. 4 and Fig. 5 are the key waveforms and frequency analyses in balanced and unbalanced situations.

As can be seen from Fig. 4 and Fig. 5, it can be verified that the mathematical derivation in (21) is correct. When in unbalanced situation, the fuel cell output current and dc-link voltage both contain twice frequency pulsating component. However, i_{fc} also leads to fuel cell output voltage pulsation.

In the next section, with the mathematical modeling for fuel cell, the effect of low frequency current ripple on fuel cell will be analyzed.

III. PEMFC MATHEMATICAL MODELING

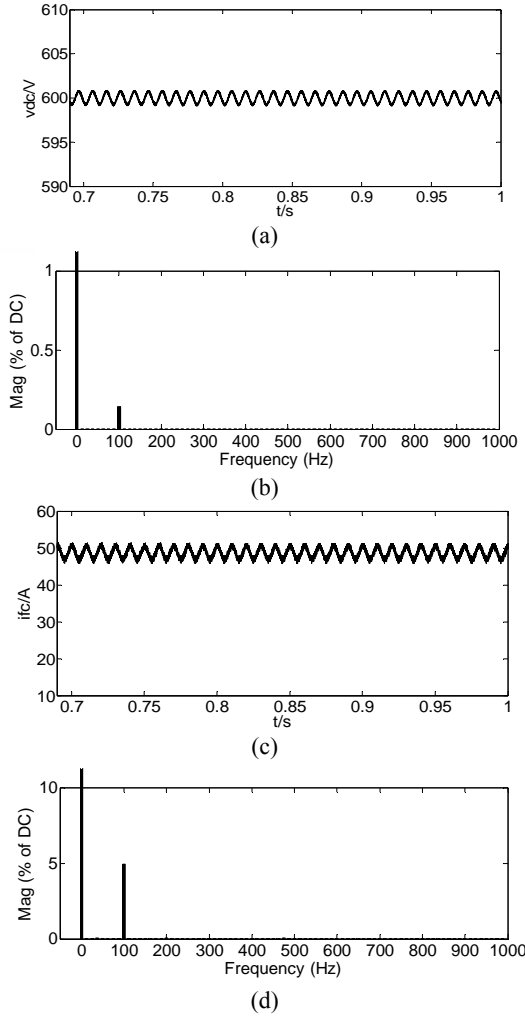As investigated in Section II, there exists low frequency

(a)

(b)

(c)

(d)

Fig. 5. Key waveforms and FFT analysis in unbalanced situation. (a) DC-link voltage v_{dc}. (b) v_{dc} FFT analysis. (c) Fuel cell output current i_{fc}. (d) i_{fc} FFT analysis.

current ripple and voltage ripple at the fuel cell side in unbalanced situation. In order to analyze the impact of these two types of ripple on fuel cell, fuel cell output characteristic model needs to be established.

The output voltage of PEMFC stack can be expressed as follows [24], [25], which is the difference between Nernst instantaneous voltage E_{Nernst} and the three types of activation overvoltage V_{act}, ohmic overvoltage V_{ohm} and concentration overvoltage V_{con}.

$$V_{st} = N(E_{Nernst} - V_{act} - V_{ohm} - V_{con}) \qquad (22)$$

Where N is the number of cells. According to [24] and [26], the Nernst voltage drop can be calculated as:

$$E_{Nernst} = E^0 + \frac{\Delta S}{2F}(T - T_{ref}) + \frac{RT}{2F}[\ln(P_{H_2}) + \frac{1}{2}\ln(P_{O_2})] \quad (23)$$

Where E^0 is the reference voltage when $T_{ref} = 273.15K$, ΔS is the standard molar entropy, F is faraday constant,
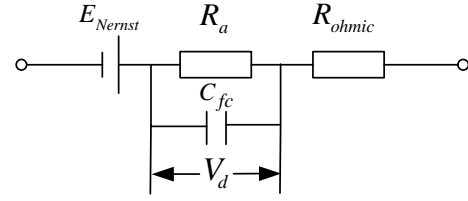

Fig. 6. Equivalent circuit of single cell.

R is gas constant, T is the operating temperature of the stack, P_{H_2} and P_{O_2} are partial pressures of hydrogen and oxygen, respectively.

When the output current is small, the activation overvoltage performs significantly. It can be written as follows by the Amphlett empirical formula:

$$V_{act} = \xi_1 + \xi_2 T + \xi_3 T \ln(c(O_2)) + \xi_4 T \ln I_{st} \qquad (24)$$

Where $c(O_2)$ is the dissolved oxygen concentration in the interface of the cathode catalyst, I_{st} is the output current, ξ_1, ξ_2, ξ_3 and ξ_4 represent model fitting coefficients based on the test data set.

$$V_{ohm} = I_{st}R_{ohmic} \qquad (25)$$

The ohmic overvoltage is shown in (25), where R_{ohmic} is the internal resistance of cell. The speed-up chemical reaction will lead to concentration overvoltage, which is defined as:

$$V_{con} = -B\ln(1 - \frac{I_{st}}{I_{max}}) \qquad (26)$$

Where B is a constant utilized in modeling the concentration overvoltage, and I_{max} is the maximum output current.

In the PEMFC, electrons gather at the electrode surface while hydrogen ions gather at the electrolyte. As a result, the phenomenon of double charge [27] generates a voltage. It can be modeled by a parallel capacitor C_{fc} at the end of the polarization resistance R_a. The capacitor can demonstrate the dynamic characteristics of the PEMFC, and the equivalent circuit is shown in Fig.6.

The output voltage of PEMFC can be rewritten as:

$$V_{st} = NE - i_{fc}N(\frac{R_a}{2R_a\omega C_{fc}+1} + R_{ohmic}) \qquad (27)$$

Substituting (21) into (27) yields:

$$V_{st} = NE - N\alpha(\frac{R_a}{2R_a\omega C_{fc}+1} + R_{ohmic})I_{dc}$$

$$-N\alpha\delta(\frac{R_a}{2R_a\omega C_{fc}+1} + R_{ohmic})i_{2nd}$$

$$-N(\frac{R_a}{2R_a\omega C_{fc}+1} + R_{ohmic})I_{dc}\alpha_{2nd} \qquad (28)$$

Based on the fuel cell output characteristic model
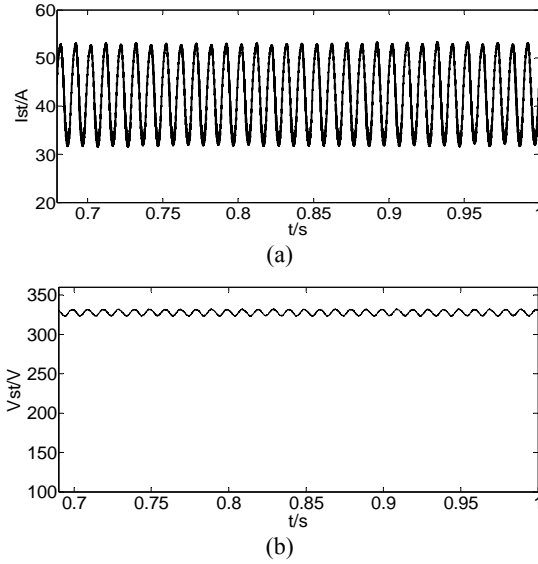
(a)

(b)

Fig. 7. Waveforms of fuel cell output current and voltage in unbalanced situation. (a) Waveform of output current. (b) Waveform of output voltage

described in (28), there is second-order voltage ripple in the fuel cell output voltage, which is shown in Fig. 7.

The ripple ratio [28] is given by:

$$\text{Ripple ratio} = \frac{ripple_{p-p}}{ripple_{average}} \times 100\% \qquad (29)$$

In Fig. 7, the ripple ratio of the fuel cell output current is as high as 39.6%, but the output voltage ripple ratio is only 1.83%. Since the reactant utilization is known to impact the mechanical nature of fuel cell, the low frequency current ripple will vary the reactant condition surrounding the cell. The high current ripple is harmful to fuel cell and will partially govern the lifespan. Thus, the current ripple needs to be kept within a small range, and the following control methods are presented to restrain the low frequency current ripple.

IV. METHODS OF LOW FREQUENCY CURRENT RIPPLE REDUCTION BASED ON CURRENT MODE CONTROL

A. Current Mode Control

Current mode control (CMC) with an outer voltage loop and an inner current loop was first proposed in [10]. It shows that CMC performs much better than single voltage loop control in reducing the low frequency current ripple of fuel cell, because the single voltage loop control only aims at stabilizing the output voltage without tracking the output current directly. With CMC, the low frequency current ripple can be greatly reduced. The dual-loop control can be shown in Fig. 8, and Fig. 9 shows the CMC control block diagram.

Where H_v is the sensor gain of the dc-link voltage, H_i is sensor gain of the fuel cell output current, $G_v(s)$ is the outer
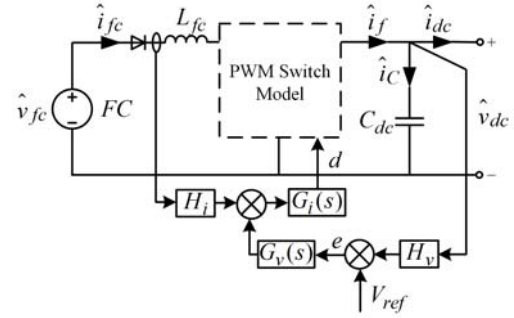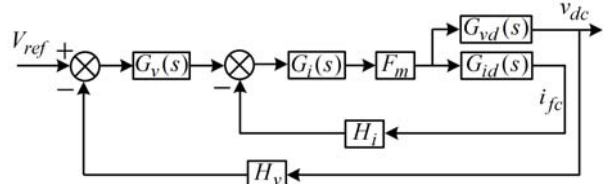

Fig. 8. Boost converter with dual-loop control.

Fig. 9. Control block diagram of CMC.

TABLE I
BOOST CONVERTER SMALL SIGNAL MODEL TRANSFER FUNCTIONS

Definition	Transfer function
$G_{id}(s) = \dfrac{\hat{i}_{fc}}{\hat{d}}$	$\dfrac{V_{dc}(2 + L_{fc}C_{dc}s)}{L_{fc}C_{dc}Rs^2 + L_{fc}s + (1-D)^2 R}$
$G_{vd}(s) = \dfrac{\hat{v}_{dc}}{\hat{d}}$	$\dfrac{RV_{dc} - \dfrac{L_{fc}V_{dc}}{(1-D)^2}s}{L_{fc}C_{dc}Rs^2 + L_{fc}s + (1-D)^2 R}$
$A_{ii}(s) = \dfrac{\hat{i}_{dc}}{\hat{i}_{fc}}$	$\dfrac{L_{fc}C_{dc}}{(1-D)}s^2 + \dfrac{L_{fc}}{(1-D)R}s + (1-D)$
$G_{vf}(s) = \dfrac{\hat{v}_{dc}}{\hat{v}_{fc}}$	$\dfrac{(1-D)R}{L_{fc}C_{dc}Rs^2 + L_{fc}s + (1-D)^2 R}$
$Z(s) = \dfrac{\hat{v}_{fc}}{\hat{i}_{fc}}$	$\dfrac{L_{fc}C_{dc}Rs^2 + L_{fc}s + (1-D)^2 R}{RC_{dc}s + 1}$
$Z_{out}(s) = \dfrac{\hat{v}_{dc}}{\hat{i}_{dc}}$	$\dfrac{RL_{fc}s}{L_{fc}C_{dc}Rs^2 + L_{fc}s + (1-D)^2 R}$
$G_{ifcv}(s) = \dfrac{\hat{i}_{fc}}{\hat{v}_{fc}}$	$\dfrac{RC_{dc}s + 1}{L_{fc}C_{dc}Rs^2 + L_{fc}s + (1-D)^2 R}$

loop voltage regulator, $G_i(s)$ is the inner loop compensation gain, and F_m is the modulator gain. $G_{id}(s)$ is the duty ratio to the inductance current transfer function, and $G_{vd}(s)$ is the duty ratio to the output voltage transfer function, which can be derived from a small signal analysis of the boost converter.

In Fig. 8, when the duty ratio is set to a fixed value, it is an open-loop converter. Table I gives the relevant small signal transfer functions, which can be derived with a Jacobin coefficient matrix.
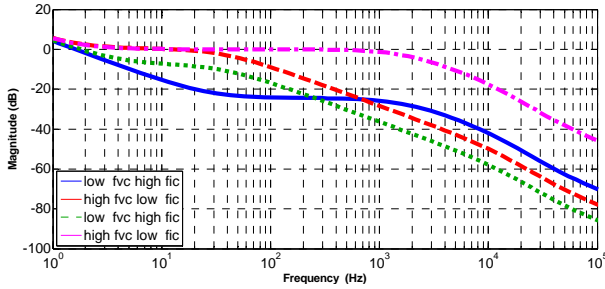
Fig. 10. $A_{cc}(s)$ magnitude-frequency diagram at different crossover frequency.

In Table I, D is the duty ratio, L_{fc} is the inductance, C_{dc} is the capacitor, and R is the equivalent load resistance. $A_{ii}(s)$ is the inductance current to the output current transfer function, $G_{vf}(s)$ is the audio susceptibility, $Z(s)$ is the input impedance, $Z_{out}(s)$ is the output impedance, and $G_{ifcv}(s)$ is the input voltage to the inductor current transfer function. In order to analyze the low frequency current ripple control capability, ripple suppression gain defined as the output voltage to the inductance current is proposed. According to Fig. 9, the ripple suppression gain of CMC can be derived as follows:

$$A_{cc}(s) = \frac{-H_v G_v(s) G_i(s) F_m G_{id}(s)}{1 + H_i G_i(s) F_m G_{id}(s)} \quad (30)$$

The compensators for the outer voltage loop and inner current loop are both based on PI controller. The outer loop and inner loop crossover frequencies must be separated clearly without overlap, in an effort to prevent the two loops from influencing each other and providing $A_{cc}(s)$ with enough attenuation in the middle frequency band. In the frequency domain, the gain of second-order frequency $2f$ is the greatest concern. The voltage loop crossover frequency should be lower than $2f$. The lower the crossover frequency is, the smaller the gain $A_{cc}(s)$ becomes, which leads to low current ripple ratio. However, the crossover frequency of the outer voltage loop is closely related to the dynamic characteristics. Thus, the relationship between the low frequency current ripple control capability and the dynamic characteristics of the converter is tradeoff. This means that a lower crossover frequency is chosen, which results in a greater low frequency current ripple reduction and a poorer dynamic performance. It also results in a high overshoot and undershoot voltage at the dc-link. In addition, the inner current loop crossover frequency is designed higher than $2f$ to guarantee ant-jamming ability.

Fig. 10 shows the gain of $A_{cc}(s)$ at different crossover frequencies. In Fig. 10, at frequency of $2f$ (100Hz), the $A_{cc}(s)$ gain of the solid line is the lowest, with a low voltage loop crossover frequency and a high current loop crossover
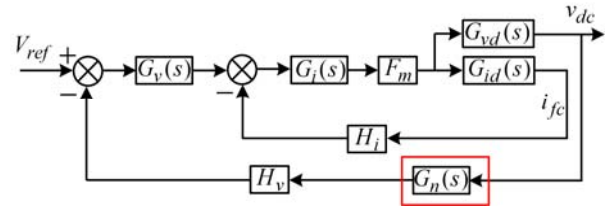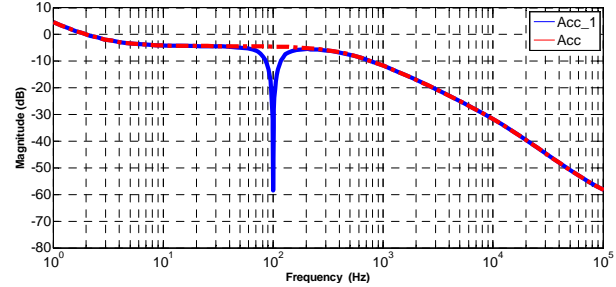

Fig. 11. Control block diagram of CMC+VLN.

Fig. 12. Magnitude-frequency diagram of $A_{cc\_1}(s)$ and $A_{cc}(s)$.

frequency. Therefore, it can theoretically achieve the greatest reduction of the low frequency current ripple.

B. Current Mode Control with a Notch Filter

In the CMC method, the low frequency current ripple can be reduced. However, from the perspective of ripple suppression gain, if the gain at frequency of $2f$ is further reduced, the controller performance is improved. A notch filter or PR-I filter with a characteristic frequency of $2f$ inserted in the outer voltage sample branch is a proper solution, which has been proposed in [29] and [30]. A control block diagram of the current mode control with a notch filter inserted in the voltage loop (CMC+VLN) method is illustrated in Fig. 11.

In the CMC method, the reference inductance current regulated by the outer voltage loop contains second-order pulsation. However, the CMC+VLN can provide ripple free reference current, which makes the outer voltage loop behave as a constant current source. Therefore, the second-order pulsation is reduced. The notch filter is given by:

$$G_n(s) = \frac{s^2 + \omega_n^2}{s^2 + \omega_n s / Q + \omega_n^2} \quad (31)$$

Here, $\omega_n = 2\pi \cdot 100 \, rad \, / \, s$ and $Q = 10$ are chosen. From Fig. 11 the ripple suppression gain of the CMC+VLN can be derived as:

$$A_{cc\_1}(s) = \frac{-H_v G_v(s) G_i(s) F_m G_n(s) G_{id}(s)}{1 + H_i G_i(s) F_m G_{id}(s)} \quad (32)$$

Fig. 12 shows the ripple suppression gain of the CMC ($A_{cc}(s)$) and CMC+VLN ($A_{cc\_1}(s)$). It can be concluded that the gain of $A_{cc\_1}(s)$ at frequency of $2f$ is much lower than that of $A_{cc}(s)$. The ripple reduction ability of the CMC+VLN is theoretically much better than that of the
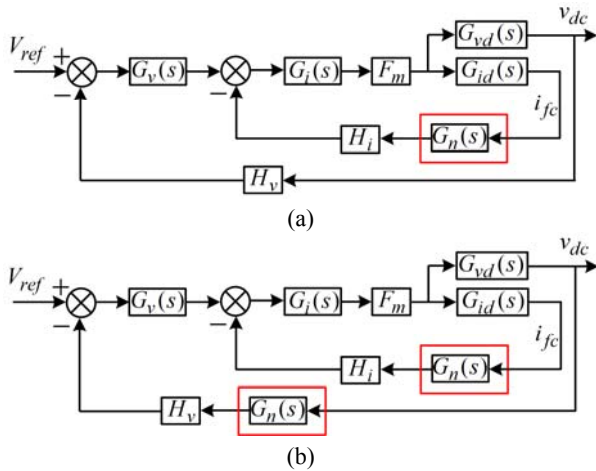
(a)

(b)

Fig. 13. Control block diagram of CMC+CLN and CMC+VCLN. (a) CMC+CLN method. (b) CMC+VCLN method.

traditional CMC method.

Based on the idea of inserting a notch filter in the voltage loop, the other two methods can be derived. They are current mode control with a notch filter inserted in the current loop (CMC+CLN), and current mode control with a notch filter inserted in both the voltage loop and the current loop (CMC+VCLN). Their control block diagrams are shown in Fig. 13.

The ripple suppression gains $A_{cc\_2}(s)$ and $A_{cc\_3}(s)$ of the CMC+CLN and CMC+VCLN derived from Fig.13 are expressed as follows:

$$A_{cc\_2}(s) = \frac{-H_v G_v(s) G_i(s) F_m G_{id}(s)}{1 + H_i G_n(s) G_i(s) F_m G_{id}(s)} \qquad (33)$$

$$A_{cc\_3}(s) = \frac{-H_v G_v(s) G_i(s) F_m G_n(s) G_{id}(s)}{1 + H_i G_n(s) G_i(s) F_m G_{id}(s)} \qquad (34)$$

In Fig. 14, the gain at a frequency of $2f$ for $A_{cc\_2}(s)$ is much higher than that for $A_{cc\_3}(s)$. Therefore, the CMC+VCLN can decrease the gain at $2f$, which is similar to the results obtained with the CMC+VLN.

Although both the CMC+VLN and the CMC+VCLN can achieve ripple free fuel cell output current, the configuration of the CMC+VLN is simpler. However, all of the above mentioned methods have poor dynamic performance. The comprehensive performance needs to be taken into account, without extra hardware costs, and eventually both low frequency current ripple reduction and dynamic performance improvement can be achieved.

V. DYNAMIC CHARACTERISTICS IMPROVEMENT BASED ON THE CMC+VLN METHOD

A. Current Feed-Forward with a Notch Filter Based on the CMC+VLN

As mentioned in [31], dynamic characteristics can be improved with a current feed-forward scheme during load
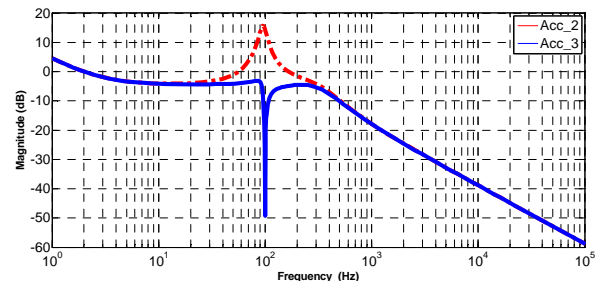

Fig. 14. Magnitude-frequency diagram of $A_{cc\_2}(s)$ and $A_{cc\_3}(s)$.
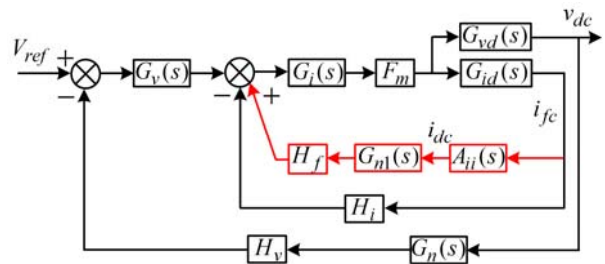

Fig. 15. Control block diagram of CMC+VLN+CFN.

transients. In order to avoid high overshoot and undershoot in the dc-link voltage, and to reduce the distortion of the ac output waveforms, the dc-link current i_{dc} treated as a load current of the dc-dc converter needs to be controlled. Since i_{dc} contains second-order component, with the current feed-forward structure, the second-order component is also added into the control loop and is not controlled by the loop. Thus, the current ripple reduction will be affected. However, with a notch filter added into the feed-forward branch, the load current feed-forward with a notch filter based on the CMC+VLN (CMC+VLN+CFN) method is achieved. A control block diagram is shown in Fig. 15.

From Fig. 15, the ripple suppression gain shown in (35) can be derived. In addition, the gain of current loop $T_{c\_l}(s)$ and the gain of the voltage loop $T_{v\_l}(s)$ are shown in Table II.

$$A_{cc\_4}(s) = \frac{-G_v(s) H_v G_i(s) F_m G_n(s) G_{id}(s)}{1 - (H_f G_{n1}(s) A_{ii}(s) - H_i) G_i(s) F_m G_{id}(s)} \qquad (35)$$

Where the parameters of $G_{n1}(s)$ are the same as those of (31), and H_f is the sensor gain of the feed-forward branch. Fig. 16 shows bode diagram of the current loop gain $T_{c\_l}(s)$ and voltage loop gain $T_{v\_l}(s)$ of the CMC+VLN+CFN as well as the current loop gain $T_c(s)$ and voltage loop gain $T_v(s)$ of the CMC+VLN.

As seen from Fig. 16, the voltage loop crossover frequency of the CMC+VLN is 1Hz, while the voltage loop crossover frequency of the CMC+VLN+CFN is 4Hz. This is larger than that of the CMC+VLN. In addition, the inner current loop crossover frequency of the CMC+VLN+CFN is 2 kHz, which is larger than that of the CMC+VLN. In theory, the dynamic

TABLE II
GAINS OF LOOP WITH CMC+VLN, CMC+VLN+CFN AND
CMC+VLN+CFBRC METHODS

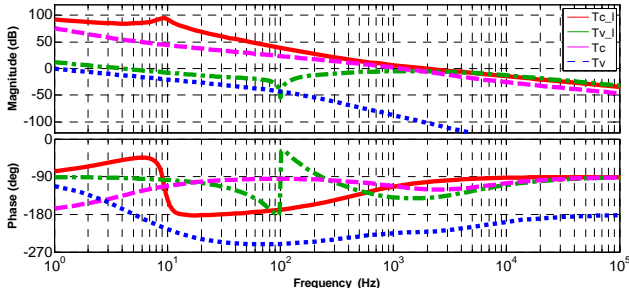| Definition	Gain
$T_c(s)$	$\dfrac{G_i(s)F_mG_{id}(s)}{1+H_iG_i(s)F_mG_{id}(s)}$
$T_v(s)$	$\dfrac{G_v(s)G_i(s)F_mG_{vd}(s)}{1+G_{id}(s)G_i(s)F_mH_i+G_v(s)G_n(s)H_vG_i(s)F_m}$
$T(s)$	$\dfrac{G_i(s)F_m}{1-G_{id}(s)G_i(s)F_m(H_fG_{n1}(s)A_{ii}(s)-H_i)}$
$T_{c\_l}(s)$	$\dfrac{G_i(s)F_mG_{id}(s)}{1-G_{id}(s)G_i(s)F_m(H_fG_{n1}(s)A_{ii}(s)-H_i)}$
$T_{v\_l}(s)$	$\dfrac{G_v(s)T(s)G_{vd}(s)}{1+G_v(s)G_n(s)H_vT(s)G_{vd}(s)}$
$T_1(s)$	$\dfrac{G_i(s)F_m}{1-G_{id}(s)F_m((G_i(s)-1)H_fG_{BPF}(s)A_{ii}(s)-G_i(s)H_i)}$
$T_{c\_ll}(s)$	$\dfrac{G_i(s)F_mG_{id}(s)}{1-G_{id}(s)F_m((G_i(s)-1)H_fG_{BPF}(s)A_{ii}(s)-G_i(s)H_i)}$
$T_{v\_ll}(s)$	$\dfrac{G_v(s)T_1(s)G_{vd}(s)}{1+G_v(s)G_n(s)H_vT_1(s)G_{vd}(s)}$

Fig. 16. Bode diagram of inner loop and outer loop for CMC+VLN+CFN and CMC+VLN.
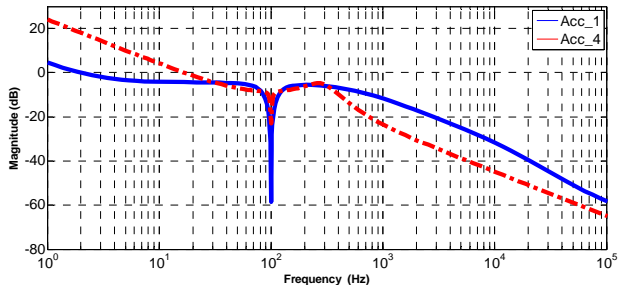
Fig. 17. Magnitude-frequency diagram of $A_{cc\_1}(s)$ and $A_{cc\_4}(s)$.

response of the CMC+VLN+CFN is better than that of the CMC+VLN.

In Fig. 17, the ripple suppression gain of the CMC+VLN and the CMC+VLN+CFN are $A_{cc\_1}(s)$ and $A_{cc\_4}(s)$, respectively. Both of them can achieve low gain at $2f$. However, the gain of the CMC+VLN is smaller, which means that the CMC+VLN is theoretically much more effective than the CMC+VLN+CFN in ripple reduction.
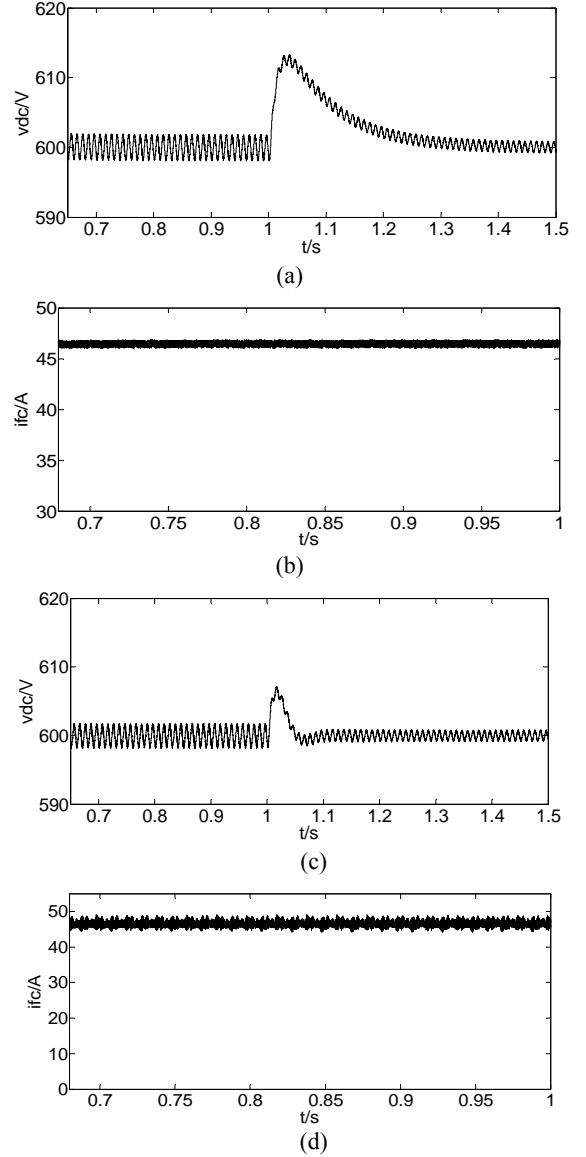

Fig. 18. Waveforms of CMC+VLN and CMC+VLN+CFN. (a) DC-link voltage with CMC+VLN method. (b) Fuel cell output current with CMC+VLN method. (c) DC-link voltage with CMC+ VLN+CFN method. (d) Fuel cell output current with CMC+ VLN+CFN method.

TABLE III
CONTROLLER PARAMETERS

CMC+VLN		CMC+VLN+CFN	
Parameter	Value	Parameter	Value
K_{p_v1}	0.099	K_{p_v2}	0.016
K_{I_v1}	0.15	K_{I_v2}	0.5
K_{p_i1}	15	K_{p_i2}	2
K_{I_i1}	0.6	K_{I_i2}	5
H_i	0.0068	H_f	0.002

Fig. 18 shows simulation waveforms of the CMC+VLN and CMC+VLN+CFN. The controller parameters are presented in Table III. K_{p_v1}, K_{I_v1}, K_{p_v2}, K_{I_v2} are the parameters of the voltage regulator, and

K_{p_i1}, K_{I_i1}, K_{p_i2}, K_{I_i2} are the parameters of the current regulator. As can be seen from Fig. 18, even though the CMC+VLN+CFN can achieve good dynamic performance, the ripple ratio of the fuel cell output current is higher than that obtained with the CMC+VLN. Therefore, in order to satisfy the two aspects, a novel control method is needed.

B. Proposed Current Feed-Forward with a Bandpass Filter Inserted and Ripple Duty Ratio Compensation Based on the CMC+VLN

As shown in (21), it is possible to obtain:

$$\alpha_{2nd} = \frac{i_{fc} - \alpha\delta i_{2nd} - I_{fc}}{I_{dc}} \qquad (36)$$

I_{fc} is the dc component of the output current of the fuel cell i_{fc}. Therefore, (36) can be rewritten as follows:

$$\alpha_{2nd} = k \cdot i_{2nd} \qquad (37)$$

Where $k = (\gamma - \alpha\delta)/I_{dc}$, and γ is the coefficient of the second-order current ripple for i_{fc}. Then it can be conclude from (37) that the inner current loop contains second-order pulsation. With a bandpass filter inserted into the current feed-forward branch, the pulsating duty ratio can be compensated. The bandpass filter G_{BPF}(s) is given by:

$$G_{BPF}(s) = \frac{\omega_n s/Q}{s^2 + \omega_n s/Q + \omega_n^2} \qquad (38)$$

Where $\omega_n = 2\pi \cdot 100 rad/s$ and $Q = 100$. A control block diagram of the proposed current feed-forward with a bandpass filter inserted and ripple duty ratio compensation based on the CMC+VLN (CMC+VLN+CFBRC) method is shown in Fig. 19.

From Fig. 19, the ripple suppression gain can be expressed by (39). The gain of the current loop $T_{c\_ll}(s)$ and the gain of the voltage loop $T_{v\_ll}(s)$ are also shown in Appendix Table II.

$$A_{cc\_5}(s) = \frac{-G_v(s)G_i(s)F_m G_n(s)G_{id}(s)}{1 + H_i G_{id}(s)F_m G_i(s) + A_{ii}(s)G_{BPF}(s)H_f G_{id}(s)F_m(1 - G_i(s))} \qquad (39)$$

Fig. 20 gives a bode diagram of the current loop gain $T_{c\_l}(s)$ and voltage loop gain $T_{v\_l}(s)$ of the CMC+VLN+CFN, as well as the current loop gain $T_{c\_ll}(s)$ and voltage loop gain $T_{v\_ll}(s)$ of the CMC+VLN+ CFBRC.

As can be seen from Fig. 20, the voltage loop crossover frequency of the CMC+VLN+CFN is 4Hz, while the voltage loop crossover frequency of the CMC+VLN+CFBRC is 3.6Hz, which is close to the CMC+VLN+CFN. This means that with the CMC+VLN+CFBRC, the dynamic performance is as good as that with the CMC+VLN+CFN. In addition, the current loop crossover frequency of the CMC+VLN+ CFBRC is 3 kHz, which is larger than that of the CMC+VLN+CFN. In Fig. 21, the ripple suppression gain of
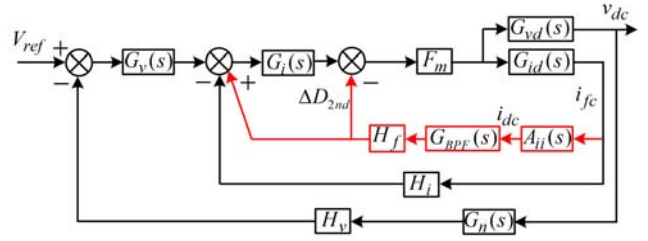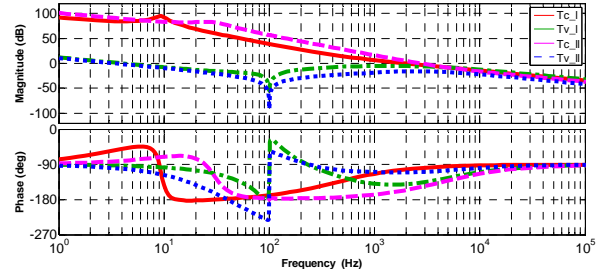

Fig. 19. Control block diagram of CMC+VLN+CFBRC.

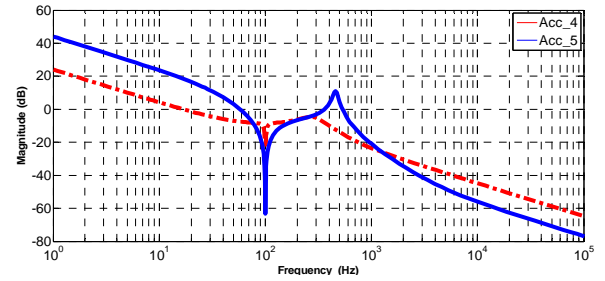Fig. 20. Bode diagram of inner loop and outer loop for CMC+ VLN+CFN and CMC+VLN+ CFBRC.

Fig. 21. Magnitude-frequency diagram of $A_{cc\_5}(s)$ and $A_{cc\_4}(s)$.

the CMC+VLN+CFBRC and CMC+VLN+CFN are referred as $A_{cc\_5}(s)$ and $A_{cc\_4}(s)$, respectively. Both of them can achieve low gain at $2f$. However, the gain of the CMC+VLN+CFBRC is much smaller. Since dynamic characteristics of the CMC+VLN+CFN are improved, the low frequency current ripple will be magnified without compensation. Moreover, with the duty ratio compensation, the CMC+VLN+CFBRC is theoretically much more effective in terms of ripple reduction than the CMC+VLN+CFN.

VI. EXPERIMENTAL RESULTS

The high power level of the PEMFC generation system makes it difficult to construct. Since the output characteristics model of the fuel cell can be simulated easily with RT-LAB, the experimental platform is set up based on RT-LAB to verify the effectiveness and accuracy of the theoretical analysis in Sections IV and V. The experimental platform is composed of a DSP TMS320F28335 controller, a RT-LAB simulator OP5600, and a computer as a real-time control interface. The experimental setup is shown in Fig. 22.
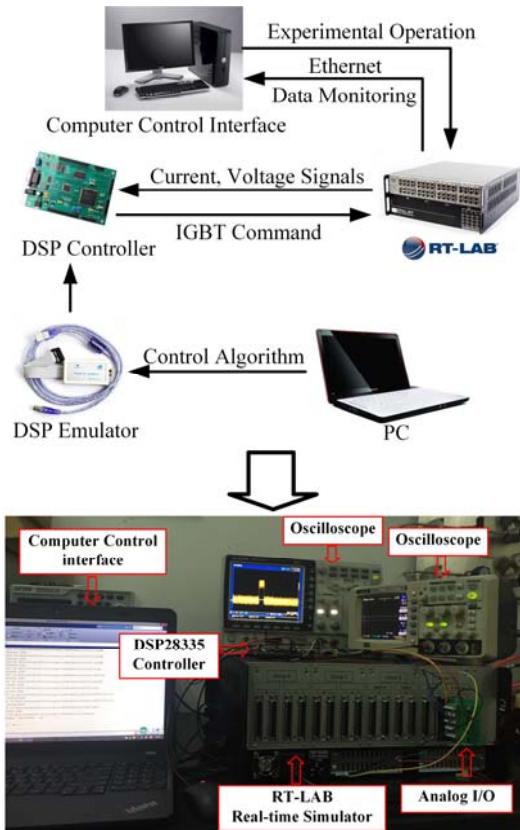
Fig. 22. Photograph of experimental setup.

TABLE IV
PEMFC STACK SPECIFICATION

Parameter	Description	Value
N	Number of cells	381
T_{fc}	Operating temperature	353.15K
T_{ref}	Reference temperature	273.15K
F	Faraday constant	96485C/mol
I_{max}	Maximum current	2.2A/cm^2
R	Universal gas constant	8.3145J/mol·K
A	Stack area	280cm^2
l	Thickness of membrane	127μm
R_c	Contact resistance between membrane and electrodes	0.14Ω

TABLE V
PEMFC GENERATION SYSTEM PARAMETERS

Parameter	Description	Value
P	Rated power	70kW
u_a, u_b, u_c	Three-phase output voltage	220V
f	Output frequency	50Hz
f_2	DC-AC switching frequency	20kHz
L_{inv}	Filter inductor of ac side	2mH
C_{inv}	Filter capacitor of ac side	125μF
C_{dc}	DC-link capacitor	900μF
V_{dc}	DC-link constant voltage	600V
L_f	DC-DC inductor	8 mH
v_{fc}	Output voltage of fuel cell	250V~350V
f_1	DC-DC switching frequency	10kHz

TABLE VI
COMPARATIVE RESULTS OF SECOND-ORDER RIPPLE REDUCTION IN STEADY-STATE

Ref	CMC	CMC+VLN	CMC+VLN+CFN	CMC+VLN+CFBRC
Ripple ratio	13.4%	4.31%	11.9%	4.37%
u_a THD	1.76%	1.76%	1.77%	1.91%
i_a THD	1.85%	1.9%	1.86%	1.82%

The DSP controller receives the physical variables, such as the voltage and current signals from the RT-LAB. After sampling by the A/D conversion units, the processed signals are then sent into the DSP TMS320F28335 where the control algorithms are discretized and the generated switching command is sent to the IGBT. Together with Matlab/Simulink and the RT-LAB control interface, the controller provides real-time control, and monitors the overall system. The parameters of the PEMFC stack and generation system are given in Table IV and V.

Fig. 23 gives steady-state experimental results of four control methods. Namely, the CMC, CMC+VLN, CMC+VLN+CFN and CMC+VLN+CFBRC. The CMC+ VLN and CMC+VLN+CFBRC are based on the CMC and CMC+VLN+CFN, respectively. The voltage loop and current loop parameters of the CMC and CMC+VLN are the same. With the load current feed-forward, the parameters of the CMC+VLN+CFN and CMC+VLN+CFBRC are regulated correspondingly. However, the voltage loop parameters and current loop parameters are also the same for the two methods. As shown in Fig. 23, the performances of CMC+VLN and CMC+VLN+CFBRC are obviously better than those of the other two methods. In addition, i_{fc} can almost achieve second-order current ripple free without pulsation. While the CMC has the worst performance in terms of second-order current ripple reduction, the CMC+VLN+CFN is better than the CMC. However, the pulsation is still very obvious. Comparative results in terms of the second-order ripple reduction of the four methods are shown in Table VI.

Fig. 24 and Fig. 25 give experimental dynamic waveforms of the four methods during load transients. It is apparent that when compared with the CMC+VLN+CFN and CMC+ VLN+CFBRC schemes, the dynamic performance of the CMC and CMC+VLN methods are poor during step-up and step-down load transients. In addition, the CMC+VLN+CFN and CMC+ VLN+CFBRC methods can achieve fast response with small dc-link voltage overshoot and undershoot, which are in agreement with the theoretical analysis. Table VII gives comparative results.
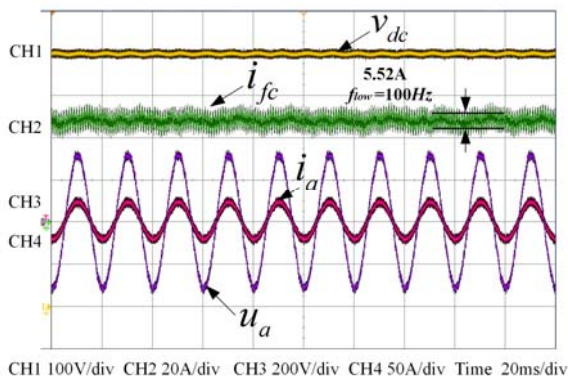
From Table VI and VII, although the CMC+VLN can achieve low ripple ratio, it shows poor dynamic performance. The CMC+VLN+CFN can realize fast response but the ripple ratio is high. Compared with the above control methods, the
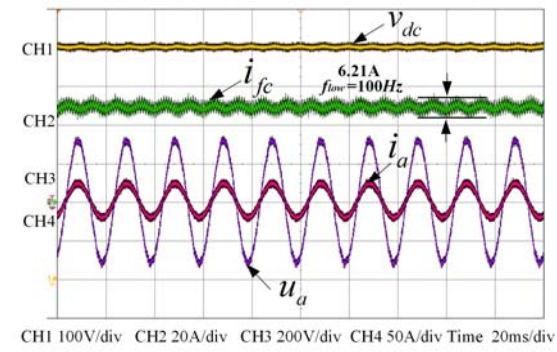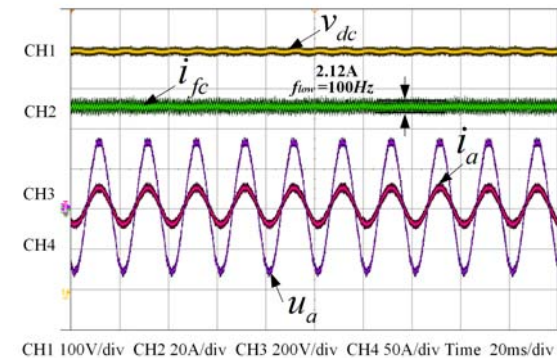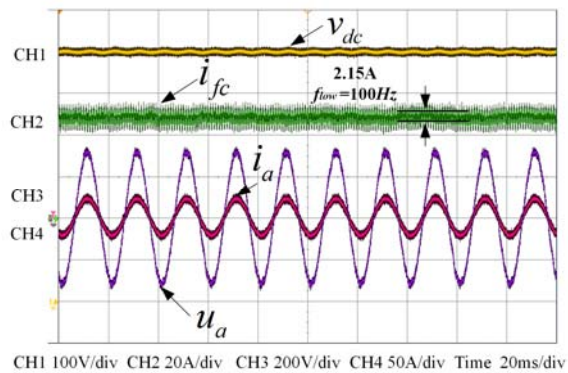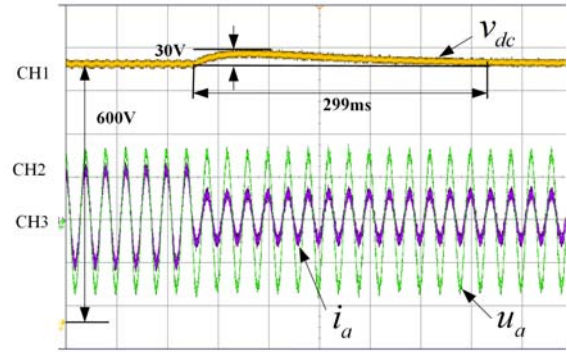
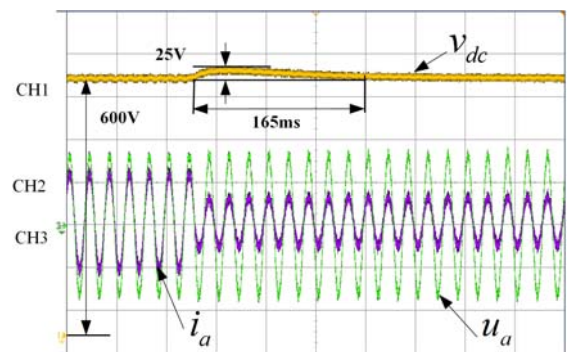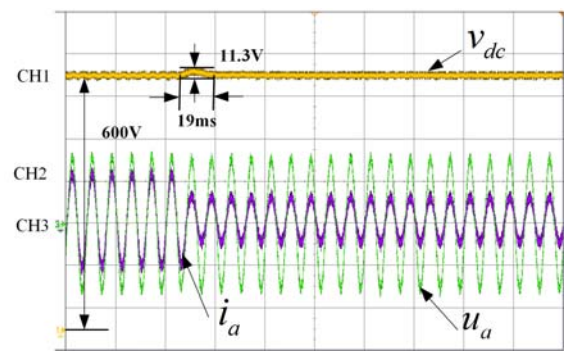Fig. 23. Experimental results of four control methods. (a) CMC. (b)CMC+VLN. (c) CMC+VLN+CFN. (d) CMC+VLN+ CFBRC.

Fig. 24. Experimental results during step-down of four control methods. (a) CMC. (b) CMC+VLN. (c) CMC+VLN+CFN. (d) CMC+VLN+CFBRC.
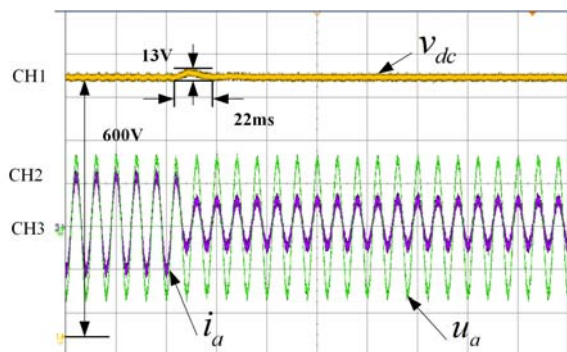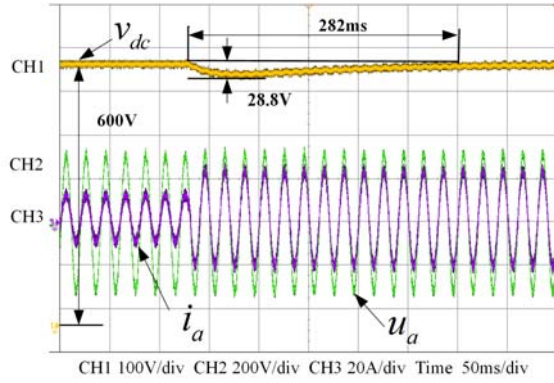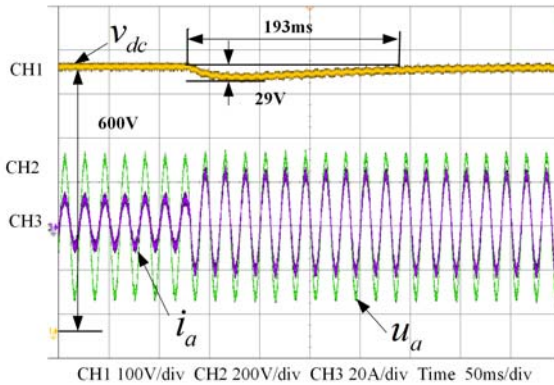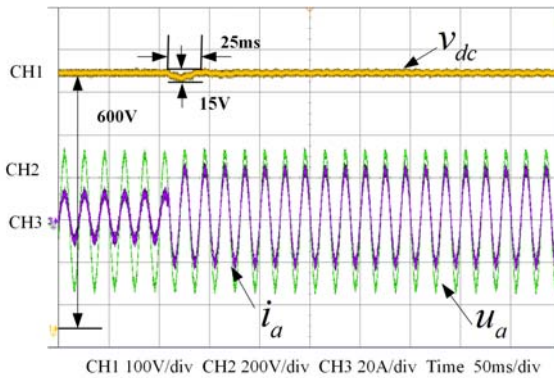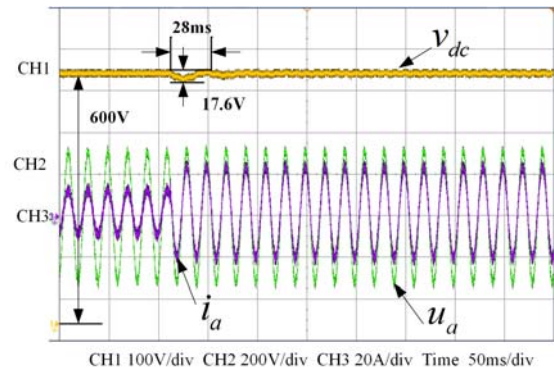
(a)

(b)

(c)

(d)

Fig. 25. Experimental results during step-up of four control methods. (a) CMC. (b) CMC+VLN. (c) CMC+VLN+CFN. (d) CMC+VLN+CFBRC.

TABLE VII
COMPARATIVE RESULTS DURING LOAD TRANSIENTS

Ref	CMC	CMC +VLN	CMC+VLN +CFN	CMC+VLN +CFBRC
Overshoot(V)	30	25	11.3	13
Undershoot(V)	28.8	29	15	17.6
Step-down setting time(ms)	299	165	19	22
Step-up setting time(ms)	282	193	25	28

proposed CMC+VLN+CFBRC can achieve both low ripple ratio and good dynamic response. In addition, its comprehensive performance is the best among the four control strategies.

VII. CONCLUSIONS

Two stage three-phase PEMFC generation systems produce second-order current ripple at the fuel cell side when the three-phase load is unbalanced. Various control methods have been studied to reduce the harmful current ripple. However, they cannot realize both low ripple ratio and fast response at the same time. In order to theoretically analyze the ripple control capability, a novel ripple suppression gain is proposed. In the meantime, in order to suppress the low frequency current ripple and to improve the dynamic response, a novel method CMC+VLN+CFBRC is proposed in this paper. A comparative study is conducted on the CMC, CMC+VLN, CMC+VLN+CFN and CMC+VLN+CFBRC. Both the theoretical analysis and experimental results demonstrate that the proposed CMC+VLN+CFBRC method can achieve a relatively fast response and low current ripple ratio. In addition, its comprehensive performance is the best among the four control methods.

ACKNOWLEDGMENT

REFERENCES

[1] J. T. Pukrushpan, A. G. Stefanopoulou, and H. Peng, "Control of fuel cell breathing," *IEEE Trans. Control Systems,* Vol. 24, No. 2, pp. 30-46, Apr. 2004.

[2] S. Jung, Y. Bae, S. Choi, and H. Kim, "A low cost utility interactive inverter for residential fuel cell generation," *IEEE Trans. Power Electron*., Vol. 22, No.6, pp. 2293-2298, Nov. 2007.

[3]   Y. Yang, X. Luo, C. Dai, W. Chen, Z. Liu, and Q. Li, "Dynamic modeling and dynamic responses of grid-connected fuel cell," *International Journal of Hydrogen Energy*, Vol. 39, No.26, pp. 14296-14305, Sep. 2014.

[4]   X. Li, W. Zhang, H. Li, R. Xie, M. Chen, G. Shen*, et al.*, "Power management unit with its control for a three-phase fuel cell power system without large electrolytic capacitors," *IEEE Trans. Power Electron.*, Vol. 26, No.12, pp. 3766-3777, Dec. 2011.

[5]   W. Choi, J. W. Howze, and P. Enjeti, "Development of an equivalent circuit model of a fuel cell to evaluate the effects of inverter ripple current," *Journal of Power Sources,* Vol. 158, No.2, pp. 1324-1332, Aug. 2006.

[6]   R. S. Gemmen, "Analysis for the effect of inverter ripple current on fuel cell operating condition," *Journal of fluids engineering*, Vol. 125, No.3, pp. 576-585, Jun. 2003.

[7]   J.-M. Kwon, E.-H. Kim, B.-H. Kwon, and K.-H. Nam, "High-efficiency fuel cell power conditioning system with input current ripple reduction," *IEEE Trans. Ind. Electron.*, Vol. 56, No.3, pp. 826-834, Mar. 2009.

[8]   B. Wahdame, L. Girardot, D. Hissel, F. Harel, X. François, D. Candusso*, et al.*, "Impact of power converter current ripple on the durability of a fuel cell stack," in *Industrial Electronics*, *2008 IEEE International Symposium on*, pp. 1495-1500, 2008.

[9]   Y. Wang, "A Novel input ripple current suppressing topology configuration and controller for residential fuel cell power conditioning system," *Journal of Fuel Cell Science and Technology*, Vol. 7, No. 3, pp. 1-3, Jun. 2010.

[10] C. Liu and J.-S. Lai, "Low frequency current ripple reduction technique with active control in a fuel cell power system with inverter load," *IEEE Trans. Power Electron.*, Vol. 22, No.4, pp. 1429-1436, Jul. 2007.

[11] S. K. Mazumder, R. K. Burra, and K. Acharya, "A ripple-mitigating and energy-efficient fuel cell power-conditioning system," *IEEE Trans. Power Electron.*, Vol. 22, No. 4, pp. 1437-1452, Jul. 2007.

[12] L. Palma, "An active power filter for low frequency ripple current reduction in fuel cell applications," in *Power Electronics Electrical Drives Automation and Motion (SPEEDAM), 2010 International Symposium on*, pp. 1308-1313, 2010.

[13] J. A. Sabate, V. Vlatkovic, R. Ridley, F. Lee, and B. Cho, "Design considerations for high-voltage high-power full-bridge zero-voltage-switched PWM converter," in *Proc. IEEE APEC*, pp. 275-284, 1990.

[14] A. Testa, S. De Caro, D. Caniglia, V. Antonucci, M. Ferraro, and F. Sergi, "Compensation of the low frequency current ripple in single phase grid connected fuel cell power systems," in *Power Electronics and Applications, 2009. EPE'09. 13th European Conference on*, pp. 1-10, 2009.

[15] R.-J. Wai and C.-Y. Lin, "Dual active low-frequency ripple control for clean-energy power-conditioning mechanism," *IEEE Trans. Ind. Electron.*, Vol. 58, No. 11, pp. 5172-5185, Nov. 2011.

[16] R. Wang, F. Wang, D. Boroyevich, R. Burgos, R. Lai, P. Ning*, et al.*, "A high power density single-phase PWM rectifier with active ripple energy storage," *IEEE Trans. Power Electron.*, Vol. 26, No. 5, pp. 1430-1443, May 2011.

[17] L. Zhang, X. Ruan, and X. Ren, "Second-harmonic current reduction and dynamic performance improvement in the two-stage inverters: an output impedance perspective," *IEEE Trans. Ind. Electron.*, Vol. 62, No. 1, pp. 394-404, Jan. 2015.

[18] G. Zhu, X. Ruan, L. Zhang, and X. Wang, "On the reduction of second harmonic current and improvement of dynamic response for two-stage single-phase inverter," *IEEE Trans. Power Electron.*, Vol. 30, No. 2, pp. 1028-1041, Feb. 2015.

[19] G. Zhu, H. Wang, C. Xiao, S.-C. Tan, and Y. Kang, "Assessment of waveform control method for mitigation of low-frequency current ripple," in *Applied Power Electronics Conference and Exposition (APEC), 2013 Twenty-Eighth Annual IEEE*, pp. 3101-3106, 2013.

[20] G.-R. Zhu, S.-C. Tan, Y. Chen, and C. K. Tse, "Mitigation of low-frequency current ripple in fuel-cell inverter systems through waveform control," *IEEE Trans. Power Electron.*, Vol. 28, No. 2, pp. 779-792, Feb. 2013.

[21] G.-R. Zhu, S.-C. Tan, K.-W. Wang, and C. K. Tse, "Waveform control of fuel-cell inverter systems," in *Energy Conversion Congress and Exposition (ECCE), 2012 IEEE*, pp. 4457-4463, 2012.

[22] A. Ale Ahmad, A. Abrishamifar, and S. Samadi, "Low-frequency current ripple reduction in front-end boost converter with single-phase inverter load," *IET Power Electronics*, Vol. 5, No. 9, pp. 1676-1683, Nov. 2012.

[23] X. Ma, B. Wang, F. Zhao, G. Qu, D. Gao, and Z. Zhou, "A high power low ripple high dynamic performance DC power supply based on thyristor converter and active filter," in *IECON 02 [Industrial Electronics Society, IEEE 2002 28th Annual Conference]*, pp. 1238-1242, 2002.

[24] J. Jia, Q. Li, Y. Wang, Y. Cham, and M. Han, "Modeling and dynamic characteristic simulation of a proton exchange membrane fuel cell," *IEEE Trans. Energy Convers.*, Vol. 24, No.1, pp. 283-291, Mar. 2009.

[25] Y. Kim and S. Kang, "Time delay control for fuel cells with bidirectional DC/DC converter and battery," *International Journal of Hydrogen Energy*, Vol. 35, No.16, pp. 8792-8803, Aug. 2010.

[26] S.-Y. Choe, J.-W. Ahn, J.-G. Lee, and S.-H. Baek, "Dynamic simulator for a PEM fuel cell system with a PWM DC/DC converter," *IEEE Trans. Energy Convers.*, Vol. 23, No. 2, pp. 669-680, Jun. 2008.

[27] F. Zenith, F. Seland, O. E. Kongstein, B. Børresen, R. Tunold, and S. Skogestad, "Control-oriented modelling and experimental study of the transient response of a high-temperature polymer fuel cell," *Journal of Power Sources*, Vol. 162, No. 1, pp. 215-227, Nov. 2006.

[28] M. V. Naik and P. Samuel, "Design and analysis of ripple current reduction in fuel cell generating systems," in *Power and Advanced Control Engineering (ICPACE), 2015 International Conference on*, pp. 200-204, 2015.

[29] J. Wang, B. Ji, X. Lu, X. Deng, F. Zhang, and C. Gong, "Steady-state and dynamic input current low-frequency ripple evaluation and reduction in two-stage single-phase inverters with back current gain model," *IEEE Trans. Power Electron.*, Vol. 29, No.8, pp. 4247-4260, Aug. 2014.

[30] H.-J. Jung, K.-S. Ha, B.-M. Song, J.-S. Lai, D.-S. Hyun, and R.-Y. Kim, "Low frequency current reduction using a quasi-notch filter operated in two-stage DC-DC-AC grid-connected systems," in *Energy Conversion Congress and Exposition (ECCE), 2011 IEEE*, pp. 2746-2750, 2011.

[31] A. V. Peterchev and S. R. Sanders, "Load-line regulation with estimated load-current feedforward: Application to microprocessor voltage regulators," *IEEE Trans. Power Electron.*, Vol. 21, No.6, pp. 1704-1717, Nov. 2006.
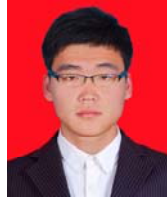
Huiwen Deng received her B.S. degree in Electrical Engineering from Southwest Jiaotong University, Chengdu, China, in 2014, where she is presently working towards her Ph.D. degree. Her current research interests include renewable energy and its applications, and fuel cell optimal control.

Qi Li received his B.S. and Ph.D. degrees in Electrical Engineering from Southwest Jiaotong University, Chengdu, China, in 2006 and 2011, respectively. He was a Visiting Scholar in the School of Electrical and Electronic Engineering, Nanyang Technological University, Jurong West, Singapore, from 2009 and 2011. He is presently working as an Associate Professor in the School of Electrical Engineering, Southwest Jiaotong University. His current research interests include the optimal controll of fuel cell locomotives, energy management strategies of hybrid systems, and power system stability and control.

Zhixiang Liu received his B.S. and M.S. degrees in Electrochemistry and Applied Chemistry from the Harbin Engineering University, Heilongjiang, China, in 1999 and 2002, respectively; and his Ph.D. degree in Chemical Engineering and Technology from Tsinghua University, Beijing,China, in 2006. He is presntely working as a Professor in the School of Electrical Engineering, Southwest Jiaotong University, Chengdu, China. His current research intrests include energy management, the optimization of fuel cells and new energy systems.

Lun Li received his B.S. degree in Electronics Engineering from Qingdao University, Qingdao, China, in 2014. He is presently working towards his M.S. degree at Southwest Jiaotong University, Chengdu, China. His current research interests include new energy technologies and their application, and fuel cell technology.

Weirong Chen received his B.S. and M.S. degrees in Electronic Engineering from the Electronic Science and Technology University, Chengdu, China, in 1985 and 1988, respectively, and his Ph.D. degree in Power Systems and its Automation from Southwest Jiaotong University, Chengdu, China, in 1998. He is presently working as a Professor in the School of Electrical Engineering, Southwest Jiaotong University. His current research intrests include renewable energy and its application, fuel cell locomotive technology, and power system control.